INESEG
INTERNATIONAL ENGINEERING SCIENCE AND EDUCATION GROUP

Middle East Journal of Science

https://dergipark.org.tr/mejs

e-ISSN:2618-6136

MEJS

Research Article

X-RAY PROPERTIES OF THE NON-COOL-CORE CLUSTER OF GALAXIES ABELL 2147

Ozden Sengul [1]

[1]Bogazici University Faculty of Education, Mathematics and Science Education Department, İstanbul, Turkey

* Corresponding author: ozden.sengul@boun.edu.tr

Abstract: *XMM-Newton data of the medium-richness non-cD cluster of galaxies Abell 2147, at a redshift of z= 0.035, were analyzed for radial distributions of its X-ray surface brightness, temperature, and metal abundances. The measured X-ray temperature is constant at 5.2 ± 0.8 keV up to ~3' (~ 130 kpc) from the center, while it decreases to ≤ 3.5 keV at ~13' (~ 600 kpc). The obtained abundance profile is consistent with being constant at 0.26 ± 0.08 times the Solar value, although a slight outward decrease is suggested. The X-ray surface brightness can be described by a single β-model, with β= 0.50 ± 0.14 and a core radius of 145" ± 45" = 105 ± 33 kpc. These properties of Abell 2147 agree with those of the best-studies non-cD cluster, Abell 1060. When compared with typical cD clusters, Abell 2147 agrees in its X-ray properties in outer regions, including in particular the outward temperature decrease. However, in the central regions (within ~ 100 kpc), Abell 2147, as well as Abell 1060, lacks major characteristics seen in many cD clusters; the temperature decrease, the abundance enhancements, and evidence for nested two scale lengths in the gravitational potential.*

Keywords: *galaxies, clusters, individual, Abell 2147, X-rays*

Received: May 16, 2020 Accepted: June 9, 2020

1. Introduction

Clusters of galaxies, each containing tens to thousands of galaxies distributed over a typical scale of ~ 1 Mpc, are considered to be the largest gravitationally bound systems in the universe. They are filled with intracluster medium (ICM), namely, the X-ray emitting hot plasma with a temperature of ~ 10^{7-8} K. The ICM, the most dominant known form of cosmic baryons, provides valuable information about the structure and evolution of the clusters of galaxies.

Clusters of galaxies can be classified based on their optical morphology [1]. One of the widely used classification schemes is the Bautz-Morgan classification, which categorizes clusters into objects of Type-I, II, and III. A Type I cluster hosts at its center a predominantly luminous elliptical galaxy, called a cD galaxy. In a Type II cluster, the brightest galaxy is intermediate between typical cD galaxies in Type I systems and normal giant elliptical galaxies. A type III cluster has many elliptical and spiral

galaxies at its core region, and none of them is either centered or dominant. Since Type III clusters lack cD galaxies, they are alternatively called non-cD clusters.

The presence of a cD galaxy in a cluster is known to systematically affect its ICM properties in the central ~ 100 kpc [2]. These include the presence of a bright cool ICM component, a clear central enhancement in the X-ray surface brightness [3], and an increased ICM metallicity. Although these phenomena were once interpreted as evidence of cooling flows [3], the interpretation was thoroughly changed by observations with ASCA [4], and with subsequent X-ray missions [5-7]. The central ICM temperature decrease in these objects is now understood as a result of the stable co-existence of hot and cool plasma [8], and the central excess brightness is considered to reflect hierarchical potential shapes around cD clusters [7,9].

Non-cD clusters, in contrast, generally lack these phenomena that are common to cD clusters. In particular, the ICM in a non-cD system is more isothermal even at the center, with weaker or no evidence of the cool component [4]. At present, the origin of the marked differences between the two types of clusters is not well understood. They may represent different stages of cluster evolution. Or else, they could be different from the beginning of their lifetime, due to fluctuations in the initial conditions of cosmological structure formation. To address this issue, we need to more thoroughly understand X-ray differences between the two cluster types. Since cD clusters have been relatively well studied, we should focus on clarifying the X-ray properties of non-cD clusters.

Abell 1060 (at a redshift of z= 0.011), with a relatively circular shape [10], is by far the best studies non-cD cluster. In addition to early ASCA results [6], recent observations of this object, with Chandra [11], XMM-Newton [12], and Suzaku [13], revealed that its ICM is nearly isothermal at ~ 3.4 keV over the central region within ~75 kpc, with a mild outward temperature decrease. Given this, it is important to examine other non-cD clusters in comparison with Abell 1060 on one hand, and with cD clusters on the other hand. Additionally, there is a recent catalogue study for clusters of galaxies which includes A2147 as well [14]. ROSAT observations showed that the global properties for temperature, morphology of the extend gas beta profile are studied and temperature and beta values are given respectively, kT = 5.2 $\pm$ 0.8 keV temperature, β= 0.50 ± 0.14 Solar, and core radius of r_c=105 ± 33 kpc consistent with the literature values for A2147 (kT = 3.81 ± 0.10 keV, β = 0.36±0.02 Solar and r_c = 85.48 ± 20.0 respectively) [14].

In the present paper, we analyzed an archival Abell 2147 (hereafter A2147), which is a nearby (z= 0.035), relaxed, non-cD cluster with a Bautz-Morgan Type III. It is devoid of a cD galaxy, and none of its three bright central galaxies coincides in position with the X-ray centroid. There is no evidence for any merging at its center. Its temperature profile was surveyed with ASCA, ROSAT, and Chandra. However, these works both dealt with a large sample of clusters, and hence information Newton data set of A2147. Utilizing the large effective area and good angular resolution of XMM-Newton, we successfully measured the temperature and abundance profiles out to a radius of ~ 600 kpc. Throughout this paper, we assume the Hubble constant to be H_o= $70h_{70}$ km s^{-1} Mpc^{-1}, and employ the cosmological parameter Ω_M= 0.27. Thus, at z= 0.035, 1' corresponds to 43.5 kpc. The Galactic line-of-sight absorption towards A2147 is taken as N_H= 3.2 x 10^{20} cm^{-2}. Unless stated otherwise, errors represent 90% confidence limits.

2. Material and Methods

2.1. XMM-Newton observation and data reduction

The present XMM-Newton observation of A2147 was carried out on 2007 August 3 for a new exposure of 12 ks. All the EPIC cameras were operated in the full-frame mode with a medium filter inserted. The data reduction and analysis were performed with the SAS version 10.0.0. For better use of Extended Source Analysis Software (ESAS), the patched versions, SAS 10.0.1 and SAS 10.0.2 were reinstalled after their release.

Unfortunately, the present data were significantly affected by soft protons. Therefore, we filtered the calibrated event files using several tasks ("mos-filter", "pn-filter" and "espfilt") in the ESAS package. These tasks identify those time periods when the proton contamination is considered to be significant, and discard all events therein. This time filtering was done in units of 100 s as a default setting. This process left us with ~ 8 ks of good time intervals out of the original 12 ks.

2.2. Subtraction of Backgrounds

Figure 1 (a) shows, in black, the 0.5-12 keV on-source spectrum, derived from the time-filtered EPIC MOS2 data within a region of radius r= 13'. For background subtraction, we first used blank-sky data sets, which we obtained from the XMM-Newton EPIC "Blank Sky" Background website where a large amount of blank-sky data of various observing conditions are available. An event file with a total exposure of 363 ks was created, under conditions of the medium filter and full-frame mode.

The red spectrum in figure 1 (a) shows the background spectrum, this accumulated over the same spatial region. The difference between the two spectra primarily represents celestial signals, including the cluster emission and the cosmic X-ray background. The two prominent features at ~ 1.49 keV and ~ 1.75 keV are both instrumental, fluorescent Al-Kα, and Si-Kα lines, respectively. The on-source spectrum becomes close to the background toward high energies. However, as shown in figure 1 (b), the former remains higher by ~30% than the latter even above ~10 keV, where the cluster emission should be negligible. This indicates that the soft proton contamination has not been completely removed by the time filtering. Presumably, prominent "flares" in the light curve were removed, while relatively constant soft protons were not.

To remove the residual soft-proton background, we resorted to another method. Namely, we created model background spectra using the "mos-back" task in the XMM-EASA package. The modeling was done for each detector and CCD individually. This ESAS-created background is shown in Figure 1 in green. Since it is mainly meant to reproduce the effects of relatively constant high-energy particles [15], it includes neither cosmic X-ray background (CXB) nor the instrumental fluorescent lines; these must be modeled separately. Although the model background thus predicts somewhat higher counts in the 10-12 keV range than the previous blank-sky data, the on-source data therein are still higher than this by a factor of ~ 1.16. Considering these, we have finally chosen to increase, by the same factor, the ESAS model.

The same analysis, performed on the MOS1 and PN data, gave Figure 2. Thus, the on source 10-12 keV MOS1 data exceed the ESAS background by a factor of ~1.5, and hence we had to increase the background by 50%. In contrast, such a background re-adjustment was not necessary for the PN data, because the ESAS background agrees well with the data over the 10-12 keV range.

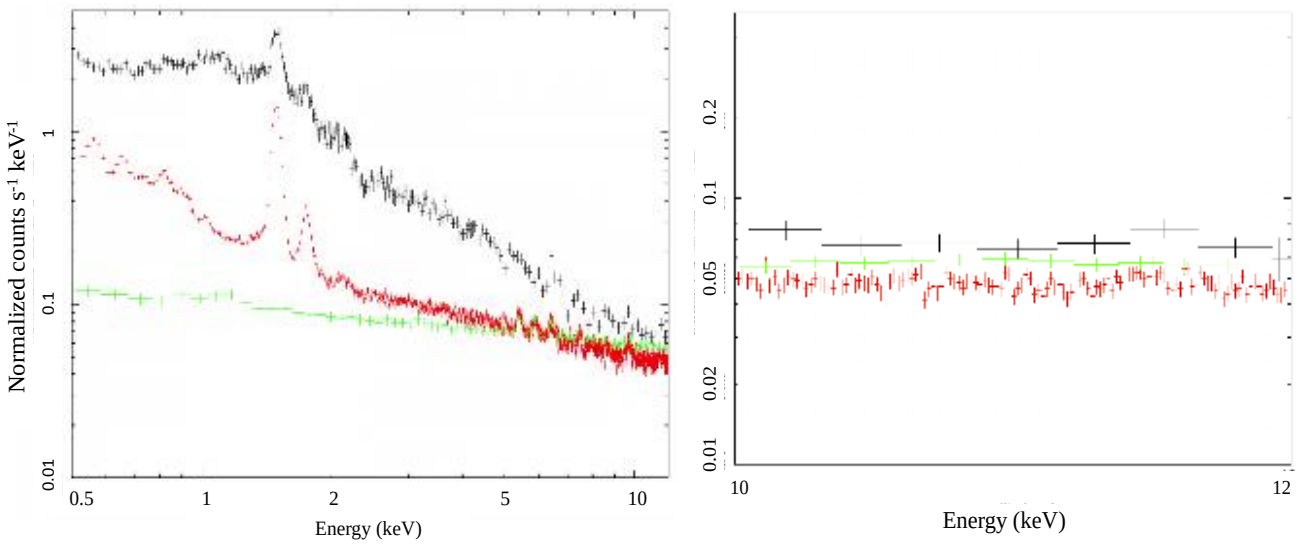

Figure 1. (Left) A raw spectrum of A2147 (black) at 0.5-12 keV, accumulated over a radius of r≤ 13' using the time-filtered MOS2 data, compared with the blank-sky background (red) and the ESAS created model background (green). Right spectrum at 10-12 keV.

The CXB contribution to our data was estimated by the "fake" command using uniform-sky response matrices, assuming that the whole sky has a uniform brightness. According to Kushino et al. (2002) [16], the CXB is characterized by a photon index of $\Gamma = 1.412 \pm 0.007 \pm 0.025$ and an average 2-10 keV brightness of $(6.28 \pm 0.04 \pm 0.64) \times 10^{-8}$ erg cm^{-2} s^{-1} str^{-1}. We hence subtracted the CXB in our data using a model that has a proton index of $\Gamma = 1.4$ and a 2-10 keV surface brightness of 6.57×10^{-9} erg cm^{-2} s^{-1} sr^{-1}, absorbed by the Galactic line-of-sight column of $N_H = 3.2 \times 10^{20}$ cm^{-2}.

The background-subtracted data are subject to both statistical (Poisson) and systematic errors. The latter is dominated by uncertainties in the level of the background to be subtracted. In Figure 1, each data point in the on-source data has a typical 1σ statistical error of ± 10%. Since we have 8 data points, the background adjustment can be done with a 1σ accuracy of ±3%. We hence quote this as the systematic error associated with the signal spectra.

2.3. Preparation of spectra

Figure 3 shows a background-inclusive 0.5-10 keV image of A2147 derived with MOS2. From the image, the X-ray center of A2147 was determined as the brightest point at (α, δ)= ($16^h02^m14.4^s$, 15^o 58' 07".50). Around this centroid, we divided the MOS1 and MOS2 images into eight concentric annular regions, with radii of 0'-1'.0, 1'.0-2'.0, 2'.0-3'.0, 3'.0-4'.5, 4'.5-5'.6, 5'.6-7'.0, 7'.0-10'.0 and 10'.0-13'.0. The innermost radii were determined considering the angular resolution of XMM-Newton (~10"), while outer regions were set progressively wider in order to approximately retain statistics.

We accumulated MOS1, MOS2, and PN spectra over the individual annuli (eight for MOS and six for PN). Then, the re-adjusted ESAS model background and the modeled CXB were subtracted. Each background-subtracted spectrum was fitted with a single APEC model, in which the temperature, abundance, and the spectrum normalization were left free. The source redshift was fixed at 0.035, and the hydrogen column density at 3.2×10^{20} cm^{-2}. To reproduce the instrumental Al-Kα and Si-Kα lines, which are present in the data but not in the employed background model, two narrow Gaussians were

added at 1.49 keV and 1.75 keV, respectively, with their normalizations left as free parameters. In this way, the MOS and PN spectra were fitted separately in 0.5-10.0 keV and 0.5-7.0 keV, respectively.

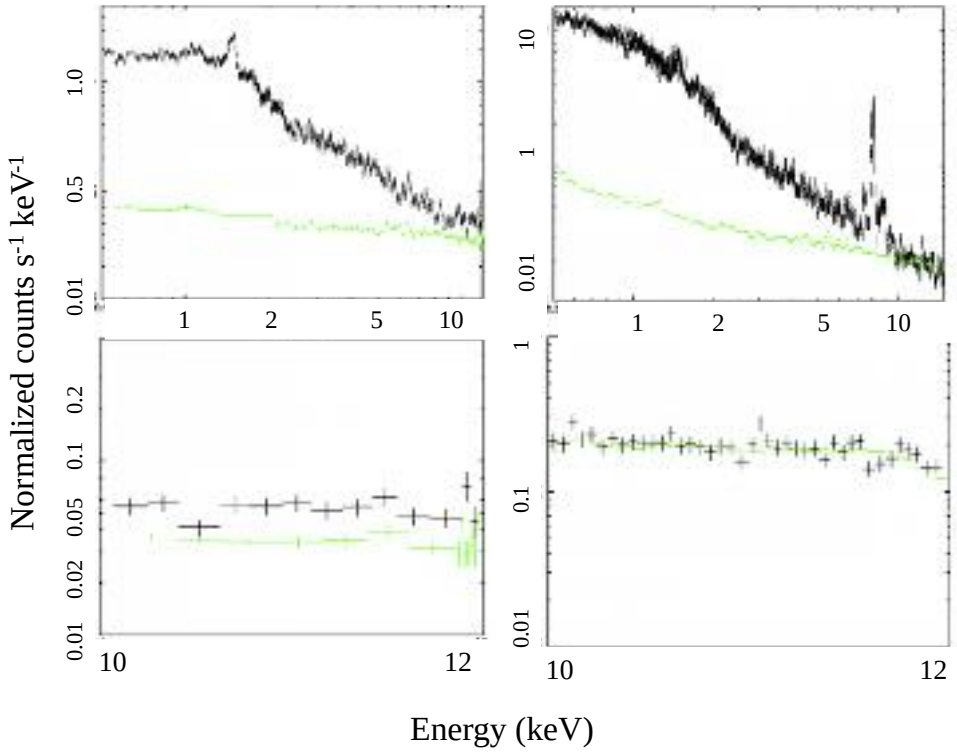

Figure 2. MOS1 (left) and PN (right) spectra (black) of A2147, both accumulated over r≤ 13', compared with the ESAS-created background (green). The bottom panel is an expanded view of the 10-12 keV region of the top panel.

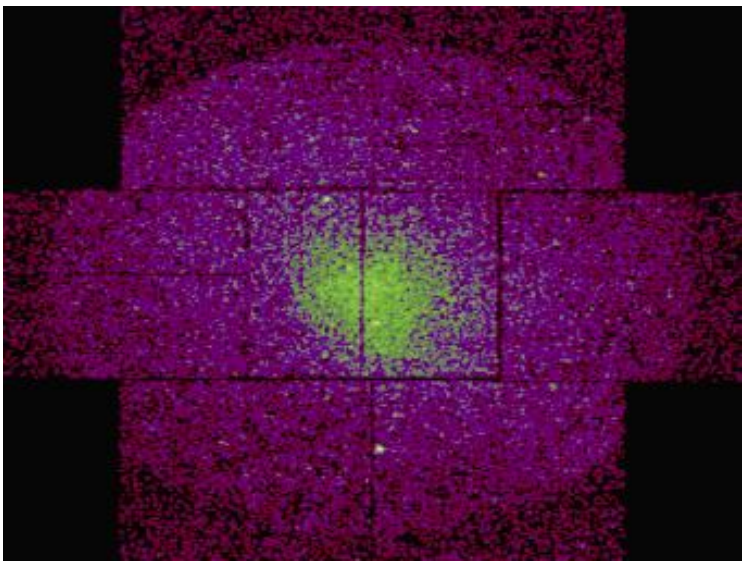

Figure 3. A background-inclusive 0.5-12 keV raw image of A2147 with MOS2.

2.4. Soft Excess Component

Several results of this single-APEC fit are shown in Figure 4. Thus, the fits were generally unacceptable; for example, the MOS2 spectra from the inner to outer annuli gave χ^2/ν= 0.91, 1.29, 1.33, 1.46, 1.36, 1.45, 1.42 and 1.76, typically with $\nu \sim 60$ degrees of freedom. As can be seen in Figure 4, the data are more concave than the model, showing "soft excess" at ≤ 1 keV.

The XMM-Newton data are often contaminated by the so-called Galactic foreground emission (or magnetospheric foreground due to Solar-wind charge-exchange) [16] which appears as a soft thermal emission in energies ≤ 2 keV with a nearly constant brightness across the EPIC FOV. Its typical intensity at 0.5 keV, ~ 1.0 cts s^{-1} keV^{-1} when integrated over the EPIC FOV much exceeds the ESAS background (~ 0.12 cts s^{-1} keV^{-1}) plus the CXB (~ 0.10 cts s^{-1} keV^{-1}). Then, the soft excess seen in Figure 4 may be caused by this phenomenon. However, we need a caution, because cool cluster emission, if any, would produce similar effects.

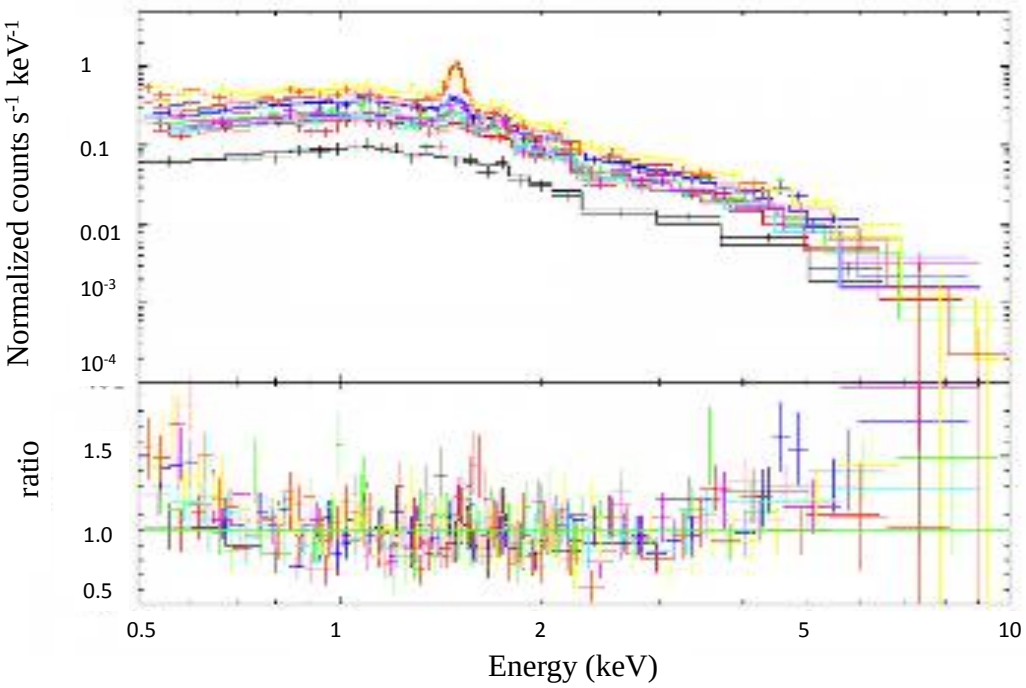

Figure 4. The individual fits the background-subtracted MOS2 spectra from the eight annular regions.

The employed model is an absorbed single APEC component. Data from the inner to outer regions are shown in black, red, cyan, green, magenta, blue, orange, and yellow. The bottom panel summarizes the data to model ratios. To examine whether the soft excess component in the present A2147 data is intrinsic to the cluster or due to a foreground (either Galactic or magnetospheric) emission, we show, in the bottom panel of Figure 4, the ratio of each annular spectrum to its best-fit model. Thus, the soft-excess strength, relative to a single thermal model approximating the cluster emission, is clearly stronger in outer regions (yellow, orange, and blue) than in inner regions (black, red, and magenta), implying that the soft excess has a much flatter brightness distribution than the ICM emission. Therefore, the soft excess must be dominated by foreground contamination, rather than by a cool component in the cluster emission.

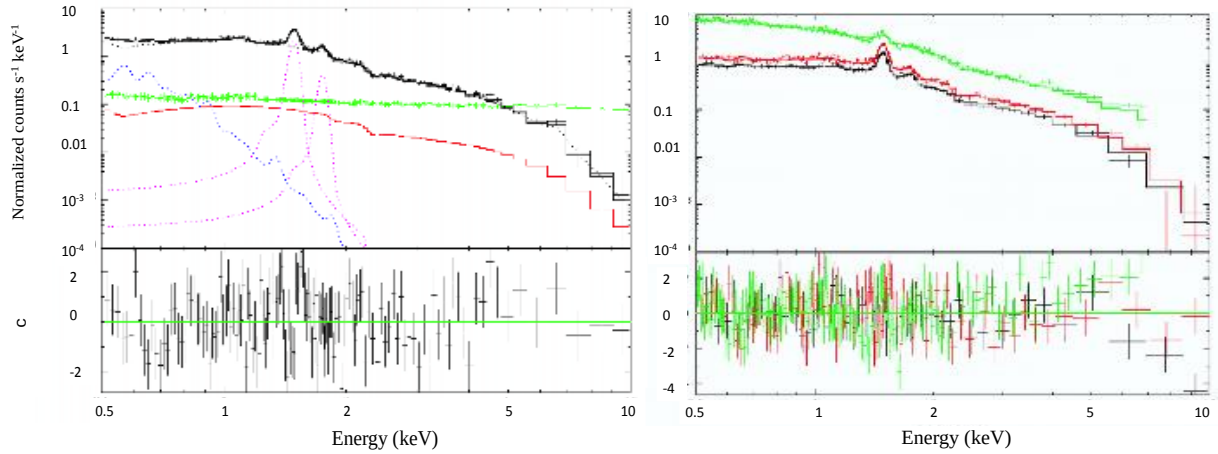

Figure 5. (a) (left) The cluster-averaged MOS2 spectrum within r = 13', decomposed into the ICM emission (black; a single APEC model), Al-Kα and Si-Kα lines (magenta), and the foreground emission (blue). The fit yielded $\chi^2/\nu = 1.12$. The ESAS background (green) and the CXB (red), which were both already subtracted before the fitting, are restored for comparison. (b) (right) MOS1 (black), MOS2 (red), and PN (green) spectra from their respective optimum regions for the soft-excess determination (excluding the core regions; see text) fitted simultaneously by a double APEC model. The two instrumental features at ~ 1.5 keV and ~ 1.75 keV are modeled by narrow Gaussians. The bottom panel shows the fit residuals.

To further quantify the soft excess component, we accumulated MOS1, MOS2, and PN spectra over radius ranges of 4'.5-13'.0, 5'.6-13'.0 and 4'.5-13'.0, respectively. To approximately maximize the statistics for the soft excess spectrum, we excluded the central region, where the ICM emission is too bright and a cool ICM emission could possibly be present. Then, the three spectra were fitted simultaneously by a double APEC model, the hotter one describing the cluster emission and the cooler one the soft excess. The two APEC temperatures, as well as the hotter APEC abundance, were allowed to float but constrained to be the same among the three spectra. The cooler APEC component was assumed to have a 1 solar abundance. The two APEC normalizations were allowed to take free values, which depend on the camera. The fit χ^2 was calculated by summing over the three spectra. As shown in Figure 5(a), the fit was acceptable ($\chi^2/\nu = 1.12$ with $\nu = 698$), and has yielded a cooler APEC temperature of 0.21 ± 0.02 keV, which is reasonable for a Galactic (or magnetospheric) foreground emission.

2.5. Cluster-averaged spectra

Now that the foreground soft excess in the present sky direction has been quantified, let us determine the cluster-averaged ICM temperature, including the bright core regions which were excluded in Figure 5(a). For this purpose, we prepared another background-subtracted MOS2 spectrum over the field of view, $r \leq 13'$, and fitted it, using a model of wabsx (apec+apec+gauss+gauss). Here again, the second APEC component represents the foreground soft excess, with a temperature fixed at 0.21 keV. Its normalization was also fixed to a value which is scaled from the fitting results of figure 5(a). Here and hereafter, the spectral fits all incorporate systematic errors by 3% of the particle background.

As shown in figure 5(b), this model has given an acceptable fit to the cluster-averaged MOS2 spectrum with $\chi^2/\nu = 1.12$ for $\nu = 698$. Similarly, the FOV-integrated MOS1 and PN spectra were fitted

successfully. The ICM temperatures and the abundances, thus determined separately by the 3 cameras, are given in the last column of table 1 and table 2, respectively. Since the three cameras thus give mutually consistent results, we also performed a simultaneous fitting to the three spectra, and again obtained a successful fit (see table 1 and table 2). The combined temperature derived from a simultaneous fitting to the three (MOS1, MOS2, and PN) spectra, 4.44 $\pm$ 0.30 keV, is consistent with the previous reports.

3. Results

3.1. Radial temperature and abundance profiles

The individual annular spectra from each camera were fitted by the same model as above, in which the soft-excess parameters are again fixed to the values determined with Figure 5(a). The innermost PN spectrum averages over 0'-3', while this range is divided into three for the MOS data. As exemplified in Figure 6, the fits were generally acceptable and yielded the fit parameters as summarized in Table 1 (the temperature and the fit chi-square) and Table 2 (the metal abundances). Finally, the spectra from the three (or two) cameras were fitted simultaneously. The results are also given in the two tables.

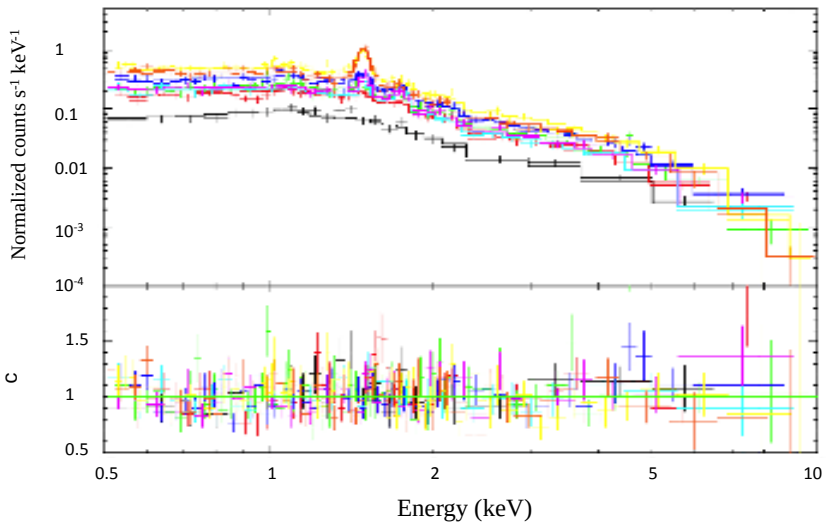

Figure 6. The individual fits the eight annular spectra of the MOS2 camera. The model describes the ICM emission with a single APEC component and the soft excess with another APEC.

Figure 7(a) shows the radial temperature profiles, determined jointly by the three (or two) cameras. Thanks to the large effective area of XMM-Newton, we have thus been able to measure the ICM temperature of A2147 up to r=13', or ~ 600 kpc. The results indicate a gradual outward temperature decline. Specifically, it is constant at 5.20 $\pm$ 0.75 keV up to r ~ 3', or 130 kpc, while it decreases to $\leq$ 3.5 keV at r ~ 13', or 600 kpc. This temperature gradient is significant because we obtain $\chi^2/\nu = 5.3$ ($\nu = 7$) if the data points in Figure 7(a) are fitted with a constant. Similarly, Figure 7 (b) shows the obtained abundance profiles, where a mild outward decrease is suggested. However, a fit to these 8 data points with a constant yield $\chi^2/\nu = 0.7$ ($\nu = 7$). Therefore, the data are consistent, within errors, with a spatially constant abundance. To be more quantitative, a power-law fit to the data points, with a function of $\alpha\ r^{\alpha}$, gave a slope as $\alpha = -0.6 \pm 0.41$, where the errors refer to 1-sigma (68%) confidence limits. Thus, $\alpha = 0$ (no gradient) is still allowed, even though the data prefer a negative slope.

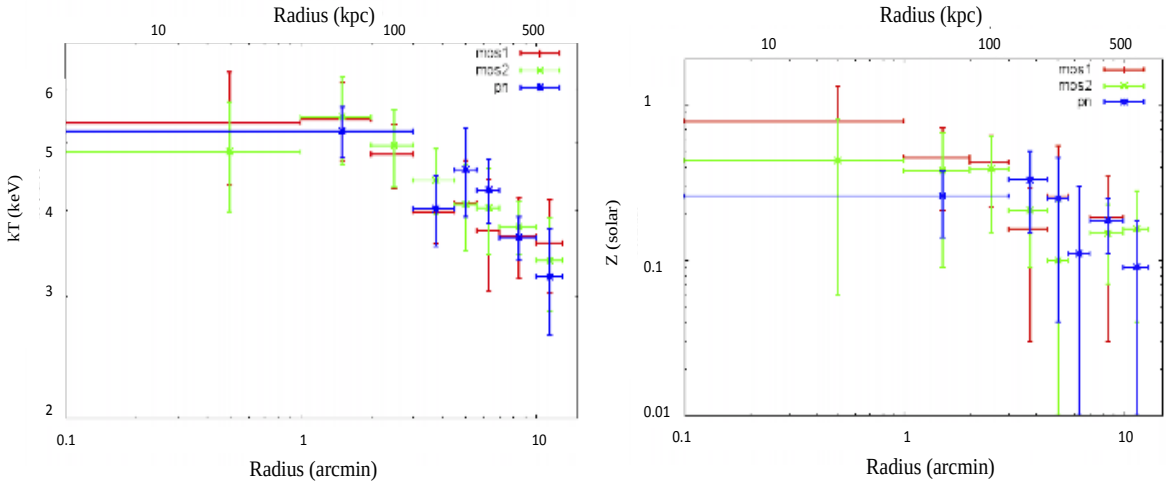

Figure 7. Temperature (panel a) and abundance (panel b) profiles of A2147, determined by joint fittings to the data of the three cameras. Errors refer to statistical (68%- 1 sigma) plus systematic ones

Table 1. The ICM temperatures measured at individual annular regions*

Radius	MOS1	χ^2/ν	MOS2	χ^2/ν	PN	χ^2/ν	Combined
0'-1'	5.34±0.99	0.80	4.86±0.88	0.89			5.08±0.93
1'-2'	5.41±0.70	1.28	5.45±0.79	1.17			5.43±0.74
2'-3'	4.81±0.51	0.78	4.95±0.64	1.12	5.20±0.44	1.10	4.86±0.58
3'-4'.5	3.98±0.41	1.11	4.42±0.48	1.07	4.01±0.47	0.94	4.11±0.45
4'.5-5'.6	4.10±0.61	0.85	4.07±0.58	0.92	4.58±0.67	0.94	4.28±0.62
5'.6-7'	3.74±0.69	0.92	4.02±0.57	1.00	4.27±0.45	1.19	4.08±0.57
7'-10'	3.67±0.49	1.37	3.78±0.33	1.02	3.65±0.26	1.20	3.69±0.36
10'-13'	3.58±0.55	1.11	3.38±0.52	1.14	3.20±0.56	1.24	3.29±0.54
0'-13'	4.62±0.28	1.08	4.21±0.28	0.99	4.48±0.35	0.98	4.44±0.30

*Errors refer to statistical plus systematic uncertainties

Table 2. The ICM abundances (Solar units) measured at individual annular regions*

Radius	MOS1	MOS2	PN	Combined
0' – 1'	0.79±0.53	0.44±0.38		0.56±0.45
1' – 2'	0.46±0.25	0.38±0.29		0.42±0.27
2' – 3'	0.43±0.21	0.39±0.24	0.26±0.12	0.41±0.22
3' – 4'.5	0.16±0.13	0.21±0.12	0.33±0.18	0.22±0.14
4'.5 – 5'.6	0.26±0.26	0.10±0.10	0.25±0.21	0.14±0.19
5'.6 – 7'	0.11±0.11	0.08±0.08	0.11±0.11	0.10±0.10
7' – 10'	0.19±0.16	0.15±0.08	0.18±0.07	0.17±0.10
10' – 13'	0.06±0.06	0.16±0.12	0.09±0.09	0.08±0.09
0' – 13'	0.24±0.12	0.21±0.06	0.34±0.07	0.26±0.08

*Errors refer to statistical plus systematic uncertainties

3.2. X-ray Surface Brightness Profiles

A surface brightness profile, extracted from an X-ray image, usually decreases monotonically from the center to the periphery and carries information on the underlying potential shape. Using the "Funtools[2] (FITS Users Need Tools)" software, we extracted the X-ray surface brightness from the background-subtracted 0.4-8 keV MOS2 image and corrected it for exposure (including the effect of

vignetting). Like in the spectrum analysis, the ESAS background was subtracted after correcting for the vignetting and multiplying by the factor of 1.16. The CXB and the foreground contributions were modeled as a constant over the FOV. The derived X-ray surface brightness profile of A2147 is shown in Figure 8. Using the β-model which is widely used in cases like this, we fitted the MOS2 surface brightness over a range of r= 0' – 13'. As shown by a solid line in Figure 8, the fit is acceptable with χ^2/ν= 0.68 (ν= 18-3= 15). Table 3 summarizes the obtained β-model parameters.

Table 3. Results of the single-β fit to the 0.4-8.0 keV surface brightness profile*

r_c	145".1± 45".0
β	0.50±0.14
χ^2/ν (ν= 18)	0.6*

*Fitted over a radius range from 0' to 13'

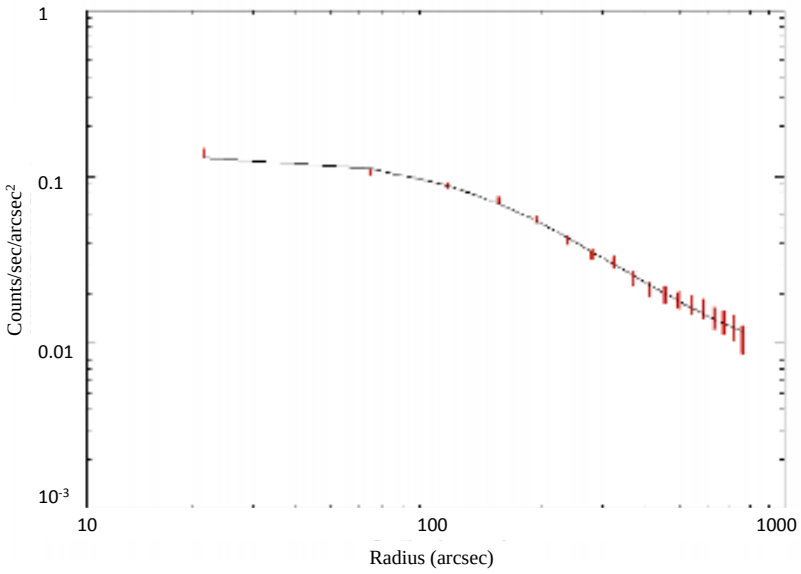

Figure 8. The 0.4-8 keV surface brightness profile of A2147 from MOS2 with statistical data plus systematical errors, fitted with a single-β model

4. Discussion

The present analysis has provided several pieces of new information about the temperature, abundance, and surface brightness distributions of XMM-Newton data of A2147. They include a significant drop in the temperature profile toward the outer radii beyond ~ 100 kpc, a loose constraint on the abundance distribution, and a successful quantification of the gravitational potential in terms of a single-β model. In this section, we will discuss these results, and compare them with those of other clusters, including Abell 1060 in particular.

4.1. Summary of results

We derived the radial temperature profile of A2147 within a radius of r= 13', (~ 600 kpc). The ICM temperature is constant at ~ 5 keV up to ~ 100 kpc, while it decreases monotonically beyond that radius, becoming ~ 3.5 keV at 600 kpc. However, its Chandra observation shows approximately

isothermal profile up to ~ 400 kpc within errors. Our results are consistent with the previous Chandra observation within the central regions as shown in Figure 9.

Then, we extracted the abundance profile for A2147 within a radius of r= 13' as shown in Figure 7. Emission-weighted abundance is 0.26 ± 0.08 solar, and best-fit values are decreasing towards outer regions. But the data are consistent, within errors, with a spatially constant abundance.

Under the assumption of the spherically symmetric distribution of the ICM, we fit the radial surface brightness profile within a radius of r= 13' with a single β-model in the energy range of 0.4-8 keV. The fitted parameters are r_{core}= 145.1 ± 45.0 arcsec= 105 ± 32.63 kpc and β= 0.5 ± 0.14. Since the surface brightness profile was described by a single β-model, the gravitational potential profile was defined by a single case length, r_c.

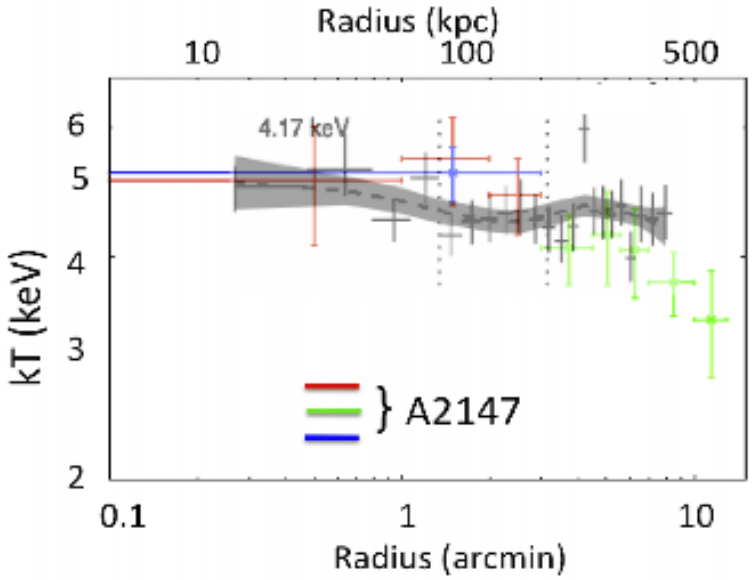

Figure 9. Comparison between A2147 and Chandra measurement

Both clusters show clear gradients for abundance profiles although both are relaxed systems without a cD galaxy.

4.2. Comparison with abundance profiles

The abundance profile of A1060 is decreasing from ~ 0.5 solar in the central region to ~ 0.2 solar in the outskirts of the cluster up to ~ 300 kpc. And, the abundance profile of A2147 is also decreasing from ~ 0.5 solar in the central region to ~ 0.1 solar in the outskirts of the cluster ~ 600 kpc.

Figure 10 shows a comparison of the abundance profiles of both clusters. Since A2147 has larger error bars, its abundance profile is consistent with being constant within errors. The figure also reveals that non-cD clusters have flatter abundance profiles than cD clusters.

4.3. Comparison with cD clusters

In addition to these, there are many differences between cD and non-cD clusters, but the origin of these differences has not been understood yet. It is well known that the temperature profile is decreasing towards the center for cD clusters within ~ 100 kpc, and there is also outward temperature decrease while the temperature profile of non-cD clusters is approximately isothermal at the center, but their outward temperature distribution has not been well known. When we compare our scaled

temperature profile with the general X-ray temperature profile for cD clusters, it is seen that cD clusters and non-cD clusters show the same temperature distribution beyond 100 kpc (Figure 11).

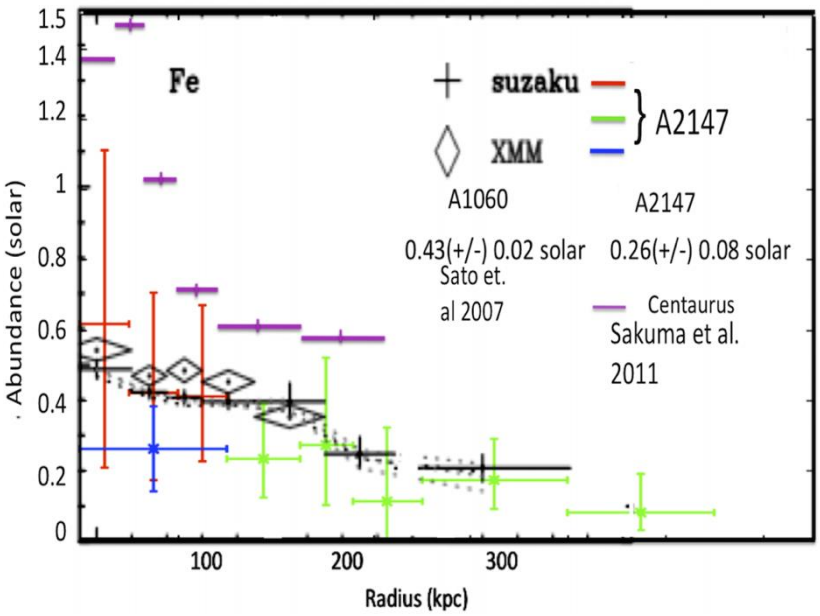

Figure 10. Comparison of A2147 abundance profile with A1060 and cD clusters

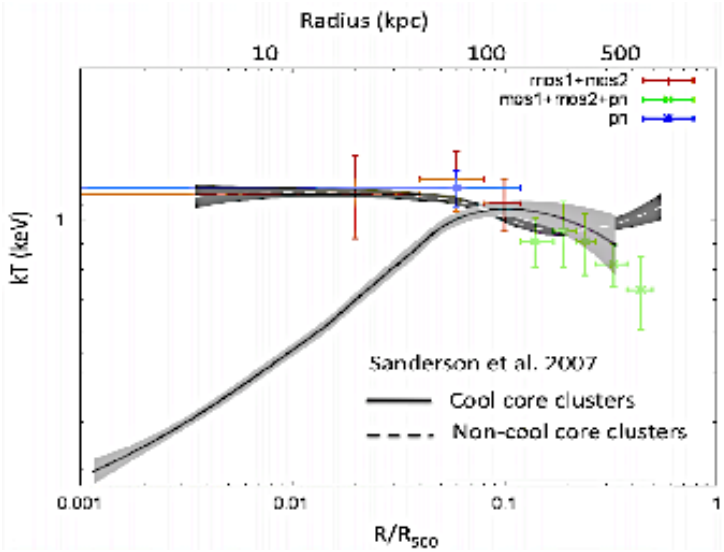

Figure 11. General X-ray temperature profile for cool-core and non-cool core clusters (Sanderson et al., 2006), comparison with A2147

4.4. Surface brightness profile

Studies show that in general, cD clusters have steeper surface brightness profile than non-cD clusters; cD clusters require double-β modeling neither single-β nor NFW model are successful. But, the surface brightness of non-cD clusters can be fitted by either double-β [13] or NFW model [18] or single-β model (as in this work). Even though both cluster types can be fitted by double-β modeling, the normalization ratio of the narrow component to a wider component is larger for cD clusters than non-cD clusters. We described the surface brightness of A2147 by a single β model with core radius of 105

kpc and β value 0.50, and its gravitational potential can be explained by a single scale length which is different from A1060.

5. Conclusion

Summing up the results presented here, let us conclude some fundamental aspects of this study. We have presented the XMM-Newton observation of the A2147 cluster of galaxies. The large effective area of XMM-Newton enables us to investigate the spatial distribution of the temperature, the metal abundance, and surface brightness in detail. We derived its temperature profile within ~ 600 kpc, it was constant at 5.2 keV in the central ~ 200 kpc, in agreement with the Chandra measurement (Sanderson et al., 2007). Beyond ~ 200 kpc, we detected mild outward temperature decrease in A2147. The overall temperature profile of A2147 was similar to that of the best-studied non-cD cluster, A1060. This temperature decreases in outer regions; observed from the two non-cD clusters, agree with those generally seen in cD clusters.

The abundance profile of A2147 confirmed that the abundance profile of non-cD clusters is inconsistent with cD clusters. The abundance profile of A2147 suggests a negative gradient similar to that of A1060, although we cannot reject a constant profile.

The gravitational potential of cD clusters usually requires two core radii because of their hierarchically nested potential shape. But, we confirmed that a single core radius of 105 kpc could describe the gravitational potential of A2147.

This scenario shows that all relaxed non-cD clusters may have similar temperature distribution in general. To confirm that studies on relaxed non-cD clusters should be supported by the data of recent satellites; observations for these specific types of clusters should be proposed for further researches.

The compliance to Research and Publication Ethics: This work was carried out by obeying research and ethics rules.

References

[1] Abell, G. O. "Clustering of galaxies", *Annual Review of Astronomy and Astrophysics*, *3*(1), 1, 1965.

[2] Jones, C., & Forman, W. "The structure of clusters of galaxies observed with Einstein", *The Astrophysical Journal*, *276*, 38-55, 1984.

[3] Fabian, A. C. "Cooling flows in clusters of galaxies", *Annual Review of Astronomy and Astrophysics*, *32*(1), 277-318, 1994.

[4] Makishima, K., Ezawa, H., Fukazawa, Y., Honda, H., Ikebe, Y., Kamae, T., ... & Takahashi, T. "X-ray probing of the central regions of clusters of galaxies", *Publications of the Astronomical Society of Japan*, *53*(3), 401-420, 2001.

[5] Kaastra, J. S., Ferrigno, C., Tamura, T., Paerels, F. B. S., Peterson, J. R., & Mittaz, J. P. D. "XMM-Newton observations of the cluster of galaxies Sérsic 159-03", *Astronomy & Astrophysics*, *365*(1), L99-L103, 2001.

[6] Tamura, T., Day, C. S., Fukazawa, Y., Hatsukade, I., Ikebe, Y., Makishima, K., ... & Yamashita, K. "Uniformity in the temperature and metallicity of the X-ray emitting gas in the Abell 1060 cluster of galaxies", *Publications of the Astronomical Society of Japan*, *48*(5), 671-677, 1996.

[7] Gu, L., Xu, H., Gu, J., Kawaharada, M., Nakazawa, K., Qin, Z., ... & Makishima, K. "Two-phase ICM in the Central Region of the Rich Cluster of Galaxies A1795: A Joint Chandra, XMM-Newton, and Suzaku View", *The Astrophysical Journal*, *749*(2), 186, 2012.

[8] Takahashi, I., Kawaharada, M., Makishima, K., Matsushita, K., Fukazawa, Y., Ikebe, Y., ... & Ota, N. "X-ray Diagnostics of Thermal Conditions of the Hot Plasmas in the Centaurus Cluster", *The Astrophysical Journal*, *701*(1), 377, 2009.

[9] Xu, H., Makishima, K., Fukazawa, Y., Ikebe, Y., Kikuchi, K. I., Ohashi, T., & Tamura, T. "Discovery of the central excess brightness in hard X-rays in the cluster of galaxies Abell 1795", *The Astrophysical Journal*, *500*(2), 738, 1998.

[10] Fitchett, Michael, and David Merritt. "Dynamics of the Hydra I galaxy cluster." *The Astrophysical Journal* 335 (1988): 18-34.

[11] Hayakawa, A., Furusho, T., Yamasaki, N. Y., Ishida, M., & Ohashi, T. "Inhomogeneity in the hot intracluster medium of Abell 1060 observed with Chandra", *Publications of the Astronomical Society of Japan*, *56*(5), 743-752, 2004.

[12] Hayakawa, A., Hoshino, A., Ishida, M., Furusho, T., Yamasaki, N. Y., & Ohashi, T. "Detailed XMM-Newton observation of the cluster of galaxies Abell 1060", *Publications of the Astronomical Society of Japan*, *58*(4), 695-702, 2006.

[13] Sato, K., Yamasaki, N. Y., Ishida, M., Ishisaki, Y., Ohashi, T., Kawahara, H., ... & Ota, N. "X-ray study of temperature and abundance profiles of the cluster of galaxies Abell 1060 with Suzaku", *Publications of the Astronomical Society of Japan*, *59*(2), 299-317, 2007.

[14] Käfer, F., Finoguenov, A., Eckert, D., Sanders, J. S., Reiprich, T. H., & Nandra, K. (2019). Toward a characterization of X-ray galaxy clusters for cosmology. *Astronomy & Astrophysics*, *628*, A43.

[15] Snowden, S. L., Mushotzky, R. F., Kuntz, K. D., & Davis, D. S. "A catalog of galaxy clusters observed by XMM-Newton", *Astronomy & Astrophysics*, *478*(2), 615-658, 2008.

[16] Kushino, A., Ishisaki, Y., Morita, U., Yamasaki, N. Y., Ishida, M., Ohashi, T., & Ueda, Y. Study of the X-ray background spectrum and its large-scale fluctuation with ASCA. *Publications of the Astronomical Society of Japan*, *54*(3), 327-352, 2002.

[17] Fujimoto, R., Mitsuda, K., McCammon, D., Takei, Y., Bauer, M., Ishisaki, Y., ... & Yamasaki, N. Y. "Evidence for solar-wind charge-exchange X-ray emission from the Earth's magnetosheath", *Publications of the Astronomical Society of Japan*, *59*(sp1), S133-S140, 2007.

[18] Tamura, T., Makishima, K., Fukazawa, Y., Ikebe, Y., & Xu, H. "X-ray measurements of the gravitational potential profile in the central region of the Abell 1060 cluster of galaxies", *The Astrophysical Journal*, *535*(2), 602, 2000.